ADVANCED OPTICAL MATERIALS
www.advopticalmat.de

Improved Mechanical Durability of High-Performance OPVs Using Semi-Interpenetrating Networks

*Zhiqi Hu, Changxu Sun, Allen Lin, Joshua Jackson, Tanguy Terlier, Damilola Owolabi, Hao Mei, Yilin Li, Yafei Wang, Siraj Sidhik, Fang Hao, Yan Yao, Aditya D. Mohite, and Rafael Verduzco**

Organic photovoltaic (OPV) devices offer a number of unique advantages over conventional single crystal silicon solar cells, such as simple and low-cost fabrication, significantly reduced weight, high flexibility, and semitransparency. However, OPV devices exhibit poor durability to mechanical deformations. Here, the use of an elastic semi-interpenetrating network is studied to improve the mechanical durability of the active layer of OPV devices based on the high-performance poly[(2,6-(4,8-bis(5-(2-ethylhexyl-3-fluoro)thiophen-2-yl)-benzo[1,2-b:4,5-b′]dithiophene))-*alt*-(5,5-(1′,3′-di-2-thienyl-5′,7′-bis(2-ethylhexyl) benzo[1′,2′-c:4′,5′-c′]dithiophene-4,8-dione)]:2,2′-[[6,6,12,12-tetrakis(4-hexylphenyl)-6,12-dihydrodithieno[2,3-d:2′,3′-d′]-s-indaceno[1,2-b:5,6-b′] dithiophene-2,8-diyl]bis[methylidyne(3-oxo-1H-indene-2,1(3H)-diylidene)]] bis[propanedinitrile] donor:acceptor blend (PBDBT-2F:ITIC). The elastic interpenetrating network is synthesized in situ through the UV photoinitiated crosslinking of thiol–ene additives in the active layer. The effects of strain as a function of bending on the network-stabilized active layer structure are systematically investigated. The elastic interpenetrating network suppresses crack formation and improves durability to high-curvature and repeated bending deformations. Performance measurements show that network-stabilized devices outperform pristine devices above a critical bending strain and number of bending deformations. The photovoltaic performance in general decreases with the increase in the network content, and the best performing devices are obtained using network forming reagents that are most compatible with the donor:acceptor system. This work describes an effective route to flexible devices using semi-interpenetrating polymer networks and provides insight into the design of the networks to maximize photovoltaic performance.

1. Introduction

Organic photovoltaic (OPV) devices possess a number of advantages over conventional, inorganic silicon-based photovoltaics. OPVs can be fabricated using industrial printing techniques and scaled to large areas.[1] They are semitransparent and compatible with lightweight and flexible substrates.[2] As a result, they have potential applications in wearable and portable sources of energy[3–5] as semitransparent, thin film coatings on windows and buildings,[6] and in biomedical applications as implantable devices.[7,8]

In order to be viable for these applications, OPVs must combine excellent electronic performance and mechanical durability.[9] A significant emphasis has been placed on improving the electronic properties of OPVs, and the power conversion efficiencies (PCEs) of the best single junction OPV devices have increased from roughly 3% in early 2000 to a current record of 18.2%.[10] This has been achieved through the development of new materials in the active layers of OPV, optimizing the processing conditions, and engineering of the device structure and interfaces. On the other hand, much less emphasis has been placed on improving the mechanical

Dr. Z. Hu, C. Sun, A. Lin, J. Jackson, H. Mei, Dr. Y. Li, Y. Wang, Dr. S. Sidhik, Prof. A. D. Mohite, Prof. R. Verduzco
Department of Chemical and Biomolecular Engineering
Rice University
6100 Main Street, MS-362, Houston, TX 77005, USA
E-mail: rafaelv@rice.edu

J. Jackson, D. Owolabi
West Houston Center for Science and Engineering
Houston Community College
MC 1524H 2811 Hayes Road, Houston, TX 77082, USA

Dr. T. Terlier
Shared Equipment Authority
Rice University
6100 Main Street, Houston, TX 77005, USA

The ORCID identification number(s) for the author(s) of this article can be found under https://doi.org/10.1002/adom.202000516.

Dr. F. Hao, Prof. Y. Yao
Department of Electrical and Computer Engineering and Texas Center for Superconductivity
University of Houston
4800 Calhoun Rd, Houston, TX 77004, USA

Prof. Y. Yao
Department of Materials Science and Engineering
University of Houston
4800 Calhoun Rd, Houston, TX 77004, USA

Prof. R. Verduzco
Department of Materials Science and Nanoengineering
Rice University
6100 Main Street, MS-325, Houston, TX 77005, USA

DOI: 10.1002/adom.202000516

properties and durability of OPV devices. Field tests are in general limited, but those that have been conducted have shown that mechanical fracture and/or delamination are crucial factors that can cause OPV device failure.[9,11–13] Mechanical failure also impacts the performance of OPV during large-scale roll-to-roll fabrication.[14,15]

The active layer of OPVs contains a blend of organic semiconductors, and most of the common active layer materials are intrinsically brittle and will fracture under strain and deformation.[16–18] This results from the rigidity and semicrystalline nature of the polymers. Small molecular blends are even more brittle than polymer-based OPVs.[11] One approach to improve the mechanical properties is to engineer the molecular structure of conjugated polymers to improve flexibility.[18–20] For example, the incorporation of conjugation-break spacers on the backbone of polymers was shown to enhance mechanical robustness of polymer film.[19,20] Another approach is to fabricate OPVs based on blends of polymeric semiconductors, which are more mechanically robust than active layer blends containing a small molecular organic semiconductor.[21] These strategies and other advances in the design of mechanically flexible organic electronic materials and devices are discussed in recent reviews.[11,18,22]

A drawback of many of the approaches is that they require modification of the structure of donor or acceptor semiconductor, which may be beneficial to mechanical flexibility but detrimental for the electronic transport in these systems. A library of small molecules and polymers that exhibit excellent electronic properties for solution-processed organic photovoltaic and other organic electronic devices has already been developed, and approaches to improve mechanical properties should ideally take advantage of these state-of-the-art materials. We recently reported network-stabilized OPVs and showed that an elastic semi-interpenetrating network formed in the active layer of an P3HT:PCBM OPV enhanced mechanical durability.[23] The elastic network was synthesized using reactive small molecular additives which can form a crosslinked thiol–ene network. The additives were codeposited with the donor and acceptor in the active layer, and the elastic network was generated in situ either through UV-irradiation or base-catalyzed thiol Michael addition coupling. We showed that up to 20 wt% of the elastic network could be incorporated without loss of power conversion efficiency and with significant suppression of cracks during stretching or bending. However, this prior study focused exclusively on the model P3HT:PCBM system, and it was unclear whether the approach presented would be applicable to high-performance OPV blends. Further, we did not study the mechanical stability of network-stabilized OPVs to bending deformations, which are likely more relevant to applications than stretching.

Herein, we present a study of network-stabilized OPVs based on the high-performance poly[(2,6-(4,8-bis(5-(2-ethylhexyl-3-fluoro)thiophen-2-yl)-benzo[1,2-b:4,5-b′]dithiophene))-*alt*-(5,5-(1′,3′-di-2-thienyl-5′,7′-bis(2-ethylhexyl)benzo[1′,2′-c:4′,5′-c′] dithiophene-4,8-dione)]:2,2′-[[6,6,12,12-tetrakis(4-hexylphenyl)-6,12-dihydrodithieno[2,3-d:2′,3′-d′]-s-indaceno[1,2-b:5,6-b′] dithiophene-2,8-diyl]bis[methylidyne(3-oxo-1H-indene-2,1(3H)-diylidene)]]bis[propanedinitrile] (PBDBT-2F:ITIC) donor:acceptor blend system (**Figure 1**). We screened four different combinations of thiol–ene reagents as semi-interpenetrating networks, which we hypothesized would improve elasticity and increase the critical strain-to-fracture of the active layer. At the same time, the additives could have a detrimental impact on morphology and/or electronic properties. For example, the additives could induce phase separation between donor and acceptor, impact crystallinity, and reduce light absorbance and charge carrier mobility. We studied the morphology, electronic properties, photovoltaic performance, and mechanical properties of network-stabilized OPVs and showed that network-stabilized devices outperform pristine devices above a critical bending strain and number of bending deformations. This work describes an effective route to high-performance flexible devices using semi-interpenetrating polymer networks and provides insight into design parameters that influence performance.

2. Results and Discussion

Our goal was to understand how an interpenetrating network in the active layer influenced electronic and mechanical properties of a high-performance OPV system, and we chose PBDBD-2F as the donor and ITIC as the acceptor. Similar donor:acceptor blends have been previously reported to give power conversion efficiencies as high as 11.2% on rigid substrates.[24] We chose four different network-forming reagents, two multifunctional thiols (pentaerythritol tetrakis(3-mercaptopropionate) (PETMP) and trimethylolpropane tris(3-mercaptopropionate) (TPTMP)) and two multifunctional "ene" reagents, one containing vinyl ether groups (pentaerythritol allyl ether (PAE)) and one containing acrylate groups (dipentaerythritol penta-acrylate (DPPA)). These thiol–ene reagents can be coupled in situ after deposition of the active layer through UV-initiated thiol radical addition or, in the case of DPPA, base-catalyzed thiol Michael addition reactions.[23] In the present study, thiol–ene networks were incorporated into the active layers by spin-casting a solution mixture of thiol–ene reagents along with PBDBT-2F and ITIC. After deposition, the active layer was thermally annealed (120 °C for 30 min) and exposed to UV light (5 min, 254 nm, 1.3 mW cm^{-2}, UVP Compact UV lamp, model UVGL-25) to crosslink the thiol–ene reagents. We previously reported residual film thickness measurements and Fourier transform infrared (FTIR) measurements that confirmed the in situ formation of an interpenetrating network.[23]

We first analyzed the impact of the interpenetrating network on the performance of bulk heterojunction OPVs fabricated on rigid ITO glass substrates through measurements of device PCEs. Our primary goal was to compare the performance of a series of devices rather than quantify the absolute PCE, and as such we did not measure external quantum efficiencies (EQEs) for each device. Nevertheless, our testing methodology followed the recommended best practices for measuring PCEs of OPVs, including using an optical mask to define the active area, repeating measurements for each device to obtain a standard deviation for the measurements, and using a filtered and properly calibrated AM 1.5 light source.[25] Pristine PBDBT-2F:ITIC devices on glass with the device structure of ITO/ZnO/PBDBT-2F:ITIC/PEDOT:poly(sodium 4-styrenesulfonate) (PSS)/Ag exhibited PCEs as high as 9.51%, significantly higher than the previously studied P3HT:PCBM devices,

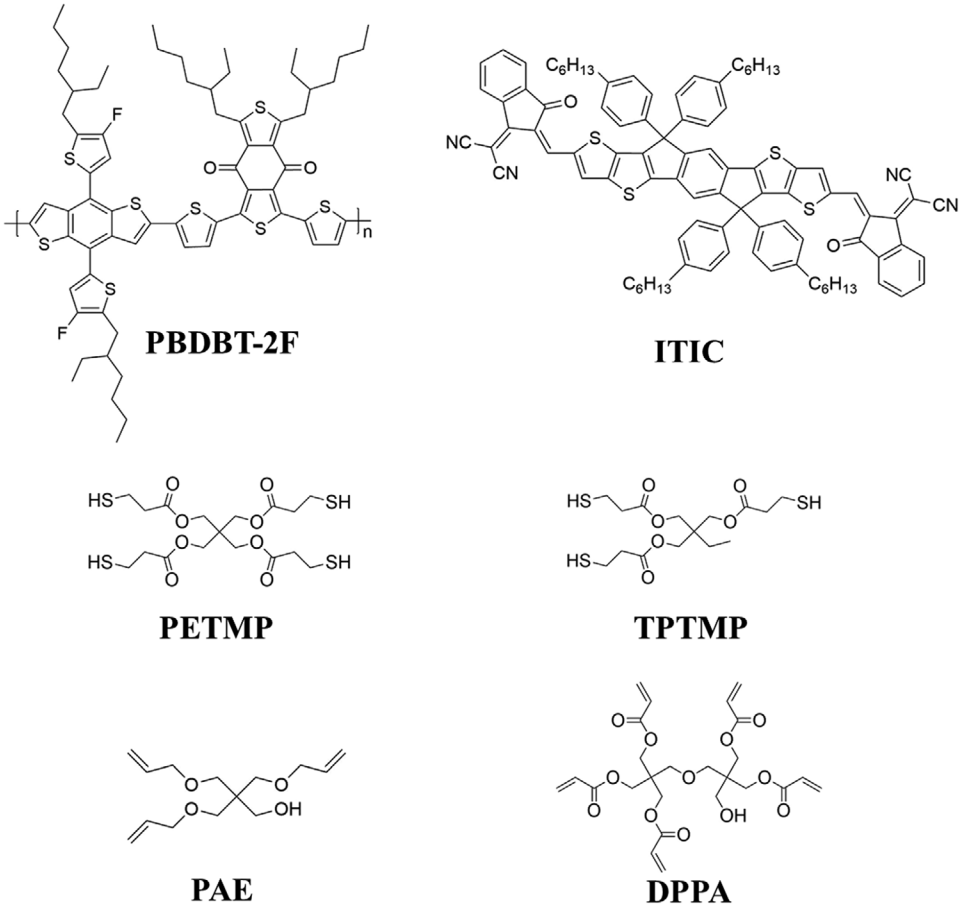

Figure 1. Molecular structures of donor PBDBT-2F, acceptor ITIC, reactive multifunctional thiols PETMP and TPTMP, and reactive multifunctional vinyl ether PAE and acrylate DPPA.

as expected. In the case of network-stabilized OPVs, we found that the PCEs decreased for all network contents. As shown in **Figure 2** and **Table 1**, with 10 wt% thiol–ene reagents added, the PCE decreased from 9.5% to 6.9% for TPTMP:PAE and to 4.7% for PETMP:DPPA. With higher contents of thiol–ene reagents, the PCE decreased further. The TPTMP:PAE formulation outperformed other formulations, and at 30 wt% thiol–ene the PCE was 1.7% for TPTMP:PAE and less than 0.1% for all other formulations studied. The film thicknesses were optimized separately for each composition of thiol–ene network, and we found that the optimal film thickness decreased with increasing thiol–ene network content. The drop in maximum PCE with increasing thiol–ene network may reflect, in part, decreased light absorption. All current–voltage curves for devices studies are provided in Figure S1 (Supporting Information).

The thiol–ene network forming materials do not absorb light, transport charges, or contribute to charge generation in the active layer, and therefore these additives are expected to have a negative effect on PCE. However, we do see important differences between P3HT:PCBM and PBDBT-2F:ITIC active layers. In our previous study, we found that up to 20 wt% thiol–ene could be incorporated in the P3HT:PCBM active layer without any loss of PCE in optimized devices, and above 20 wt% the PCE decreased rapidly. As shown in Figure 2, in the PBDBT-2F:ITIC system the PCE decreased with thiol–ene content across the entire composition range tested for all thiol–ene formulations. The stronger sensitivity of the PBDBT-2F:ITIC system to thiol–ene content is likely related to the much higher photocurrents and internal

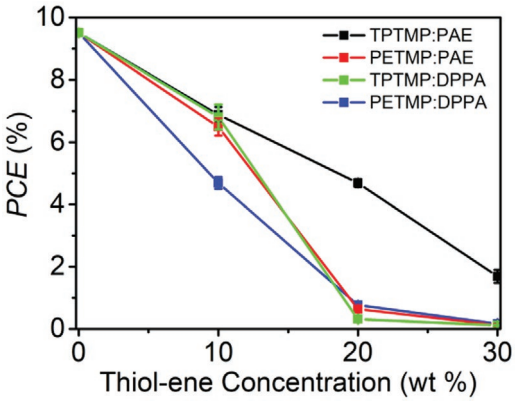

Figure 2. Power conversion efficiencies (PCEs) for OPV devices with network stabilized OPVs at various thiol–ene concentrations coated on ITO glass substrate. Each datapoint represents an average over five devices, and error bars reflect standard deviations. Error bars are not visible for some points because they are smaller than the markers.

Table 1. Power conversion efficiencies (PCE), fill factors (FF), short-circuit current (J_{SC}), and open-circuit voltage (V_{OC}) for network stabilized OPVs at varying thiol–ene network content on ITO-coated glass substrates averaged over five sample tests. Standard deviations are shown in parentheses.

Network components	Thiol–ene content [wt%]	PCE [%]	FF [%]	J_{sc} [mA cm^{-2}]	V_{oc} [V]
N/A	0	9.51 (0.06)	48.02 (1.14)	21.22 (0.66)	0.94 (0.01)
TPTMP:PAE	10	6.88 (0.25)	39.62 (0.42)	20.48 (0.68)	0.85 (0.01)
	20	4.69 (0.13)	33.21 (1.99)	17.42 (0.58)	0.82 (0.04)
	30	1.69 (0.21)	23.46 (3.06)	9.92 (0.58)	0.74 (0.05)
PETMP:PAE	10	6.49 (0.28)	42.45 (1.47)	16.20 (0.15)	0.95 (0.01)
	20	0.64 (0.05)	17.43 (1.32)	4.86 (0.27)	0.78 (0.07)
	30	0.13 (0.04)	16.12 (0.88)	1.03 (0.26)	0.75 (0.03)
TPTMP:DPPA	10	6.81 (0.40)	40.67 (1.85)	18.43 (1.07)	0.91 (0.01)
	20	0.32 (0.02)	16.29 (1.71)	3.58 (0.23)	0.58 (0.06)
	30	0.12 (0.01)	16.21 (2.10)	1.52 (0.14)	0.54 (0.07)
PETMP:DPPA	10	4.69 (0.19)	32.64 (1.04)	16.27 (0.33)	0.88 (0.02)
	20	0.77 (0.05)	17.23 (0.69)	7.35 (0.26)	0.60 (0.01)
	30	0.17 (0.02)	17.20 (0.92)	2.07 (0.24)	0.49 (0.03)

photoconversion efficiencies of PBDBT-2F:ITIC relative to the P3HT:PCBM system. Recombination losses are significant in the P3HT:PCBM system, accounting for up to 17% losses in PCE as reported previously.[26] A significant fraction of the domains in P3HT:PCBM bulk heterojunction active layer are poorly ordered and/or inactive in the photovoltaic process. The PBDBT-2F:ITIC system exhibited significant PCE losses even at 10 wt% thiol–ene additives, reflecting that a greater proportion of the active layer is active in the photovoltaic process.

The results presented in Figure 2 and Table 1 also reveal a significant dependence on the specific thiol–ene reagents chosen. Formulations with TPTMP:PAE performed the best across the composition series, while PETMP:DPPA performed poorest. We hypothesized that these differences could be attributed to varying mixing compatibilities of the thiol–ene reagents with the PBDBT-2F:ITIC donor:acceptor blend. Poorly compatible additives would have a stronger detrimental effect on the active layer morphology and performance. To test this hypothesis, we quantified the interfacial free energy between each thiol–ene reagent and the donor–acceptor film. Specifically, we measured the contact angle of each network-forming reagent on a film of PBDBT-2F:ITIC as shown in Figure S2 (Supporting Information) and used pendant drop measurements to measure the surface energies of the network-forming reagents. The contact angle measurements were conducted using the pure thiol–ene reagents in liquid form deposited on top of a PBDBT-2F:ITIC film. These values were used to calculate the interfacial free energy, given by $\Delta G_i = -\gamma_L \cos(\theta)$, where γ_L is the surface energy of the liquid and θ the contact angle between cross-linker materials and the PBDBT-2F:ITIC film. ΔG_i represents the change in interfacial energy of the surface in contact with the test liquid relative to the interfacial energy with air and provides an estimate of the compatibility of each component with the PBDBT-2F:ITIC blend. The results of these measurements are provided in **Table 2**. We observed significant differences in the interfacial energies of the different reagents with the donor–acceptor film. In particular, PETMP and DPPA are the least compatible thiol and "ene" reagents, respectively, as reflected in the larger contact angles and smaller magnitude of ΔG_i. PAE and TPTMP are the most compatible reagents studied. The measured interfacial energies trend with the observed impact of the different combinations of additives on PCE shown in Figure 2. For example, our measurements indicate that PETMP and DPPA have the least favorable interfacial energy and are least compatible with the donor–acceptor system. TPTMP and PAE are the most compatible and produce devices with the highest relative PCE among the various thiol–ene reagents tested. This supports our hypothesis and also provides a simple approach for developing and screening new additives for network-forming additives.

Table 2. Contact angle on PBDBT-2F:ITIC bulk heterojunction films, liquid surface energy, and free energy of immersion for PAE, DPPA, TPTMP, and PETMP liquids.

	Component	Contact angle [°]	Surface energy [mN m^{-1}]	Interfacial free energy [mN m^{-1}]
Ene/acrylate	PAE	22.7	30.55 ± 0.04	−28.19
	DPPA	53.6	32.56 ± 0.04	−19.32
Thiol	TPTMP	53.6	35.71 ± 0.01	−21.19
	PETMP	66.7	38.40 ± 0.03	−15.19

We conducted atomic force microscopy (AFM) measurements to analyze the morphology of the top of the active layer with network forming reagents. AFM is an established technique for investigating surface morphology in bulk heterojunction OPVs[27] and has been recently used to study both crystallinity and phase separation in PBDBT:ITIC blends.[28] Blends of PBDBT-2F:ITIC with thiol–ene reagents were deposited on glass and exposed to UV light, using procedures identical as for OPV device fabrication. As shown in **Figure 3**, AFM revealed phase-separated domains of increasing size at the top of the film with increasing thiol–ene concentration. While these domains at the top of the film may not be representative of the bulk film morphology, we previously used a combination of differential scanning calorimetry and grazing-incidence wide-angle X-ray scattering measurements in a different active layer system and found bulk morphological changes in active layer films with increasing contents of thiol–ene additives.[23] We also conducted time-of-flight secondary ion mass spectroscopy (ToF-SIMS) measurements of the active layer film on glass, as shown in Figure S3 (Supporting Information). These measurements revealed the distribution of PBDBT-2F through the depth of the film across the various formulations tested.

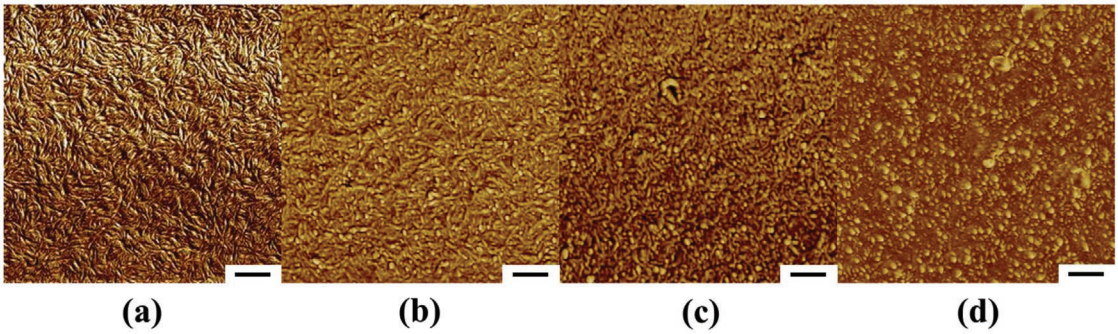

Figure 3. AFM phase image for PBDBT-2F:ITIC film with TPTMP:PAE thiol–ene at various percentage and spin rate coated on glass substrate. a) 0% thiol–ene spin-coated under 2500 rpm, 20 s. b) 10% thiol–ene spin-coated under 4000 rpm, 20 s. c) 20% thiol–ene spin-coated under 4000 rpm, 20 s. d) 30% thiol–ene spin-coated under 4000 rpm, 20 s. Scale bar = 300 nm.

In the pristine devices, the PBDBT-2F was enriched near the bottom substrate, which was more favorable for device performance. In thiol–ene stabilized films, the PBDBT-2F migrated toward the top of the film. Furthermore, through UV–vis measurements shown in Figure S4 (Supporting Information), we observed significant changes in the absorbance features, which suggest significant morphological changes with changing thiol–ene concentrations.[29,30]

In order to understand the impact of the thiol–ene network on mechanical properties, we first conducted measurements of crack onset strain for active layers under uniaxial deformation. To perform these measurements, the active layers were cast on glass and then floated off and transferred to a polydimethylsiloxane (PDMS) substrate. The PDMS substrate was deformed while monitoring the formation of cracks in the active layer by polarizing optical microscopy, and we compared the stretching profiles for active layer with TPTMP:PAE, PETMP:PAE, TPTMP:DPPA, and PETMP:DPPA networks. A representative example of these measurements is shown in **Figure 4** for TPTMP:PAE thiol–ene additives ranging from 10 to 30 wt%,

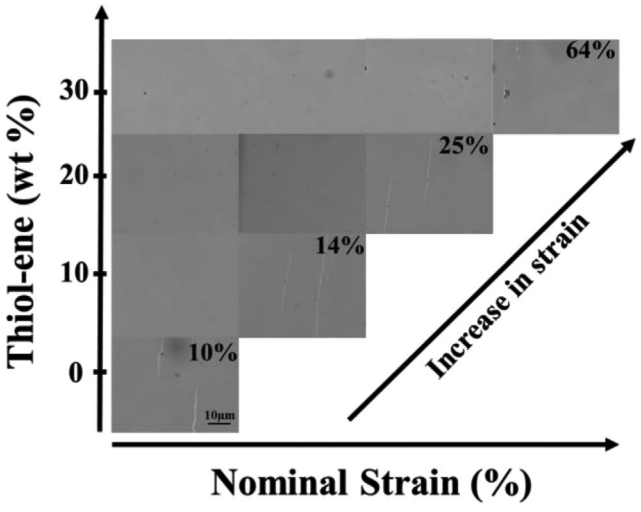

Figure 4. Optical micrographs for network stabilized PBDBT-2F:ITIC with varying concentration of TPTMP:PAE network at different elongational strains. Unlabeled images in column 1–3 represent profile images at 10%, 20%, and 30%, respectively. Scale bar = 10 μm.

and measurements for other formulations are provided in Figure S5 (Supporting Information). Cracks that formed in the active layer were readily visible by optical microscopy, and we saw a clear and significant increase in the crack onset strain with increasing thiol–ene content. We observed this improved mechanical durability across all thiol–ene formulations tested. The measured crack onset strains are provided in **Table 3**.

While uniaxial mechanical deformations give insight into the mechanical durability of the OPV devices, bending deformations are more relevant to applications since devices are commonly bent or rolled during or after processing.[14] To investigate the stability of OPV devices under bending deformations, we fabricated OPV devices on thin and flexible polyethylene naphthalate (PEN) substrates. The device structures consisted of ITO as the bottom electrode, a layer of ZnO as the electron transport layer, the PBDBT-2F:ITIC active layer (1:1 mass ratio), PEDOT:PSS as the hole transport layer, and thermally evaporated silver as the top electrode. The processing approach used for devices on glass was modified slightly for devices fabricated on PEN substrates, and a detailed description of fabrication methods for PEN substrates is provided in the Experimental Section. We focused exclusively on the TPTMP:PAE system to stabilize OPV devices on PEN since it outperformed the other formulations. The resulting devices were found to produce power conversion efficiencies as high as 8.27% for PBDBT-2F:ITIC active layer with no added thiol–ene. The PCE decreased with increasing TPTMP:PAE content, as expected, as shown in **Table 4** and Figure S1 (Supporting Information). The PCEs for devices on PEN are within 20% of those fabricated on glass, and we observed a similar trend in the decrease in PCE with increasing thiol–ene content. In addition to a decrease in the short-circuit current J_{SC} and fill factor FF, we also observed

Table 3. Measured crack onset strains for blends of thiol–ene/thiol–acrylate stabilized PBDBT-2F:ITIC films.

Cross-linker [wt%]	Crack onset strain [%]			
	PETMP:DPPA	TPTMP:PAE	PETMP:PAE	TPTMP:DPPA
0	10	10	10	10
10	21	14	13	13
20	29	25	28	17
30	42	64	82	23

Table 4. Power conversion efficiencies (PCE), fill factors (FF), short-circuit current (J_{SC}), and open-circuit voltage (V_{OC}) for network stabilized OPVs at varying thiol–ene network content on ITO-coated PEN substrates averaged over five sample tests. Standard deviations are shown in parentheses.

Thiol–ene content [wt%]	Best PCE [%]	Average PCE [%]	FF [%]	J_{sc} [mA cm^{-2}]	V_{oc} [V]
0	8.27	8.16 (0.05)	41.94 (1.19)	20.42 (0.45)	0.96 (0.01)
10	5.85	5.60 (0.08)	39.59 (0.94)	16.53 (0.06)	0.86 (0.02)
20	4.84	4.45 (0.14)	34.24 (1.37)	16.48 (0.50)	0.79 (0.02)
30	1.82	1.52 (0.09)	22.08 (0.59)	9.05 (0.39)	0.76 (0.03)

a significant drop in the open-circuit voltage V_{OC}. While the source of this drop in V_{OC} is unclear, this may be related to changes in the morphology and/or composition of the donor–acceptor interface and intermolecular packing in the donor or acceptor phases. For example, prior studies on P3HT-based OPVs have shown that vertical stratification can produce similarly large changes in the V_{OC}.[31] Evidence for vertical stratification of PBDBT-2F toward the top electrode with the addition of thiol–ene networks was provided by ToF-SIMS measurements, as shown in Figure S3 (Supporting Information). We also observed an increase in contact resistance with increasing TPTMP:PAE content, as reflected in the change in slope of the current–voltage traces. This may also be related to vertical stratification of PBDBT-2F toward the top electrode.

We conducted bending tests by wrapping the devices around cylindrical rods with curvature of 0.72, 1.36, and 2.11 cm^{-1}, as shown in Figure S6 (Supporting Information). We subjected each device to 50 bend deformation cycles, bending and unbending the device for each cycle. The resulting normalized PCEs relative to the undeformed devices are shown in **Figure 5** and absolute PCE values are provided in **Figure 6**. At the lowest bending curvature tested, bending curvature of 0.72 cm^{-1}, we saw modest losses in PCE with bending and the greatest loss in PCE for unstabilized OPV, with a drop by about 15%. At the same bending curvature, devices with 10 wt% TPTMP:PAE exhibited a reduction in PCE by ≈5%. For devices with 20 and 30 wt% TPTMP:PAE, we observed an increase in PCE with bending. We believe this may be due to chain alignment induced by strains in the thiol–ene network, and we discuss this hypothesis in more detail below.

When the bending curvature was increased to 1.36 cm^{-1}, we observed significant PCE losses for most devices. The PCE dropped by 40% after one bending cycle, and subsequent losses in PCE were more gradual for subsequent bending cycles. The unstabilized OPV devices only retained ≈15% of their initial PCE after 50 bending cycles. By comparison, the 10 and 20 wt% network-stabilized devices retained 50% of the initial PCE after 50 bending cycles. This was a significantly higher fraction compared with unstabilized devices and corresponded to greater PCEs in absolute terms after 50 bending cycles. The OPV devices with 30 wt% network content retained ≈90% of their PCE after 50 bending cycles. We also observed an initial increase in PCE after the first several bending cycles, followed by a graduate loss of PCE with further bending.

At the highest bending curvature, all devices lost significant PCE after bending. The loss was most significant for the first few bending cycles. For example, unstabilized OPVs lost 80% of their normalized PCE after one bending cycle. By comparison, the 30 wt% network-stabilized OPVs exhibited an increase in PCE after the first cycle, followed by a consistent and more gradual decrease in PCE with bending. At the two highest bending curvatures, all network-stabilized OPV devices outperformed pristine OPV devices after 50 bending cycles in terms of absolute PCE (Figure 6).

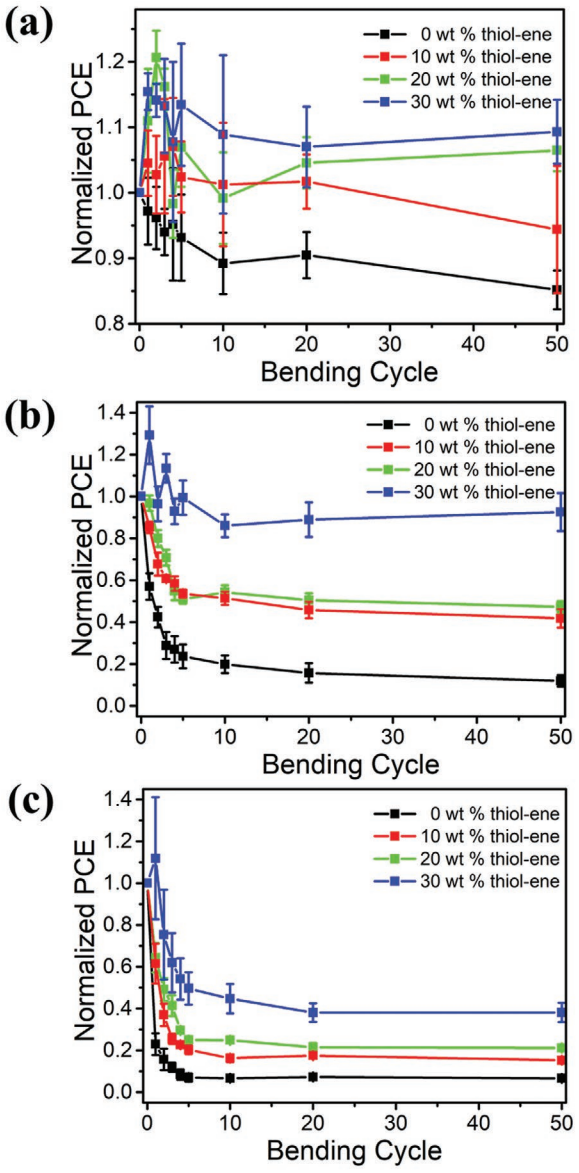

Figure 5. a–c) Normalized efficiency for TPTMP:PAE stabilized photovoltaic device on PEN substrate with varying bending cycles at bending curvature of 0.72, 1.36, and 2.11 cm^{-1}.

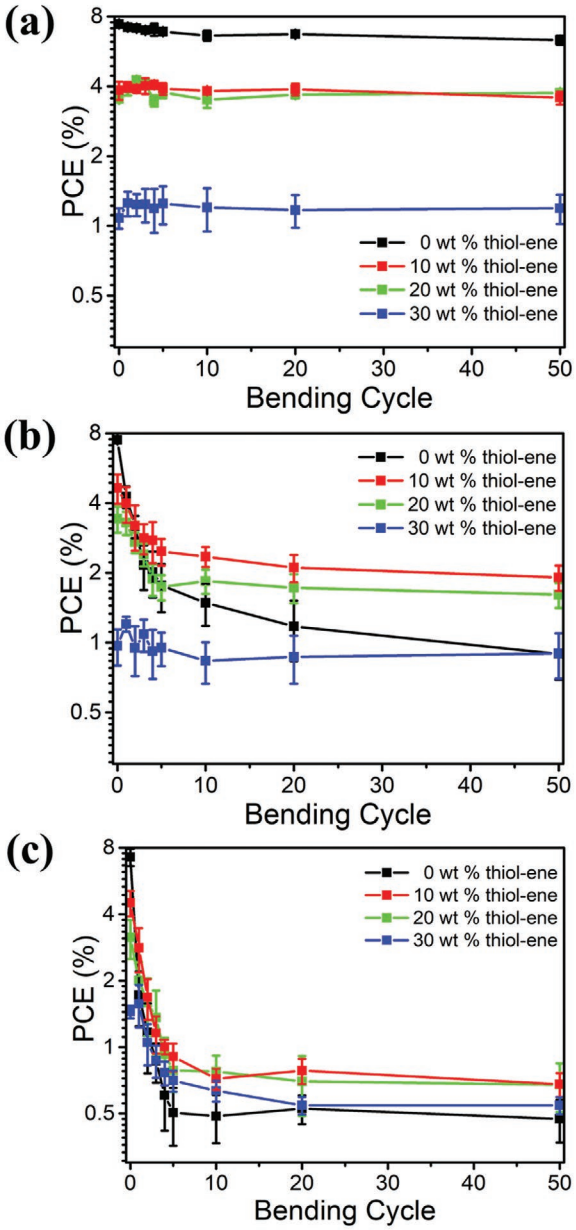

Figure 6. a–c) Power conversion efficiency (PCE) for pristine and TPTMP:PAE network-stabilized photovoltaic device on PEN substrate with varying bending cycles at bending curvature of 0.72, 1.36, and 2.11 cm^{-1}.

We consistently observed an increase in PCE with bending for all 30 wt% network stabilized OPV devices and in some 10 and 20 wt% stabilized devices. For the smallest curvature, this produced devices with higher PCEs than the initial undeformed devices. The PCE was observed to increase followed by a decrease with continued bending. This increase in PCE with bending was unexpected and is not fully understood, but we propose that this may be attributed to improved chain alignment induced by network strains. The thiol–ene network will change the rheological properties of the active layer and may produce viscoelastic effects that improve chain alignment. A higher degree of chain alignment can improve electronic properties of the active layer.[32] We conducted AFM measurements on the 30 wt% network stabilized OPV devices before bending, after 10 bending cycles, and after 50 bending cycles and observed mesoscopic features (≈10 µm) aligned along the primary direction of strain for network-stabilized devices as shown in Figure S7 (Supporting Information).

These data can also provide a critical bending threshold above which PCE degrades. This threshold is higher for OPV devices with higher thiol–ene network contents. The drop in PCE after one bending cycle is shown for all network contents and bending curvatures tested in **Figure 7**. For each device formulation, we observed a threshold bending curvature above which the PCE degraded significantly with just one bending cycle. For example, the efficiency for device with 0% thiol–ene decreased after one bending cycle with a curvature of 0.72 cm^{-1}, but for devices with 20 wt% thiol–ene a drop in PCE was observed only for curvatures greater than ≈1.20 cm^{-1}. The data in Figure 7 also clearly show the increase in PCE after one bending cycle for all network-stabilized OPVs after one bend deformation.

These measurements show that thiol–ene interpenetrating networks improved the mechanical robustness of OPV devices and, over a range of network concentrations and bending radii, produced devices with PCEs greater than unstabilized devices. Specifically, OPV devices with 10 or 20 wt% thiol–ene outperformed unstabilized OPV devices for bending curvature of 1.36 cm^{-1} or greater. As shown in Figure 7, the use of a semi-interpenetrating network delayed the onset of performance degradation to higher bending curvatures.

3. Conclusions

We studied the use of an elastic semi-interpenetrating network to improve the mechanical durability of the active layer of OPV devices based on the high-performance PBDBT-2F:ITIC donor:acceptor blend. While all thiol–ene networks were detrimental to PCE, the impact varied widely across four different compositions tested, and compatibility of the network-forming reagents with PBDBT-2F:ITIC correlated with the resulting impact on performance. Under mechanical deformation, both stretching and bending, semi-interpenetrating networks can improve mechanical stability. The incorporation of

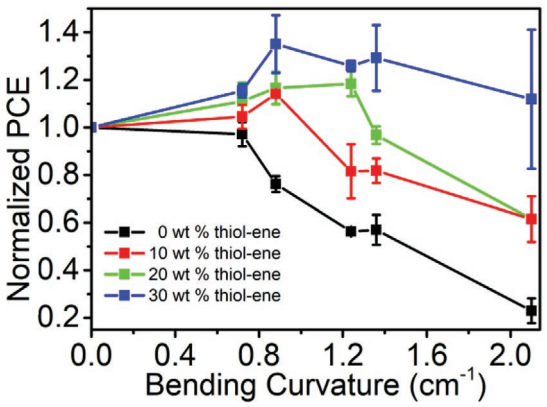

Figure 7. Normalized efficiency for TPTMP:PAE network stabilized OPV devices at varying bending curvature after one bending cycle.

a semi-interpenetrating network delayed the onset of performance degradation to higher bending curvatures, and over a range of network compositions and bending deformations tested, stabilized OPV devices outperformed pristine OPVs. This work describes an effective route to performance flexible devices using semi-interpenetrating polymer networks and provides insight into the design of the interpenetrating networks to improve mechanical durability and maximize photovoltaic performance.

4. Experimental Section

Materials: PETMP (Sigma-Aldrich, >95%), TPTMP (Sigma-Aldrich, ≥95%), PAE (Sigma-Aldrich, 70%), DPPA (Sigma-Aldrich), PBDBT-2F (1-Material), ITIC (1-Material), PSS (Sigma-Aldrich, $M_w \approx 70$ kg mol^{-1}), zinc acetate dehydrate (Sigma-Aldrich, ≥98%), 2-methoxyethanol (Sigma-Aldrich, ≥99.3%), ethanolamine (Alfa Aesar, >99%), and 184 silicone elastomer kit (base and curing agent, Dow Sylgard) were obtained from commercial suppliers and used as received.

Fabrication of Network-Stabilized Bulk Heterojunction Active Layers: Three different thiol–ene/thiol–acrylate solutions were made based on a 1:1 molar ratio of thiol and ene/acrylate functional group. 1) PETMP (50 mg, 0.10 mmol, 0.41 equiv thiol) and PAE (50 mg, 0.14 mmol, 0.41 equiv vinyl ether), 2) PETMP (54 mg, 0.11 mmol, 0.44 equiv thiol) and DPPA (46 mg, 0.088 mmol, 0.44 equiv acrylate), 3) TPTMP (52 mg, 0.13 mmol, 0.39 equiv thiol) and PAE (48 mg, 0.13 mmol, 0.39 equiv vinyl ether) were mixed, respectively, and dissolved in 1 mL of chlorobenzene with 0.3% 1,8-diiodooctane (DIO) to make three 100 mg mL^{-1} stock solutions. Each thiol–ene solution was further diluted to a concentration of 20 mg mL^{-1}. Inside a nitrogen-filled glovebox, 20 mg mL^{-1} of active layer stock solution was made by dissolving PBDBT-2F (30 mg) and ITIC (30 mg) in 3 mL of chlorobenzene (0.3% DIO) and the solution was heated and stirred at 65 °C for 12 h. The diluted thiol–ene/thiol–acrylate solution and the active layer stock solution were mixed at a desired ratio to achieve a targeted thiol–ene network composition in the active layer. The blend solution was stirred for 12 h at room temperature, and then was spin-coated on a substrate and exposed to UV short-wave irradiation (254 nm, 1.3 mW cm^{-2}, UVP Compact UV lamp, model UVGL-25) for 5 min to initiate cross-linking.

Fabrication of OPVs on ITO Glass and ITO-Coated PEN: Organic photovoltaic devices were fabricated in an inverted structure: substrate/ITO/ZnO/active layer/AI 4083/Ag cathode. Precursor solution ZnO was prepared by dissolving 1 g of zinc acetate dehydrate in 10 mL of 2-methoxyethanol with 0.28 g of ethanolamine as a surfactant. 1 mL of PEDOT:PSS Clevios P VP AI 4083 (Heraeus) was diluted in 10 mL of isopropanol to make an AI 4083 solution. The substrate (1 in. × 1 in.) used in device fabrication is either ITO glass or 0.125 mm thick ITO-coated PEN substrate. Detailed substrate preparation was demonstrated in Figure S8 (Supporting Information). Each substrate was then washed by ultrasonication sequentially in 0.5% Hellmanex III (Helma) in DI water, DI water, acetone, and isopropanol for 15 min and dried in an oven at 90 °C for 1 h. The substrate was treated with UV–ozone for 15 min followed by spin-coating ZnO solution at 2000 rpm for 40 s and then annealed at 200 °C for 1 h. The substrate was transferred into a nitrogen-filled glovebox. The active layer blend solution was spin-coated on top of the ZnO layer at 4000 rpm for 20 s and then cross-linked under short-wave UV for 5 min followed by annealing at 120 °C for 30 min. The substrate was then allowed to cool to room temperature inside the glovebox. PEDOT:PSS solution was spin-coated on top of the active layer at 4000 rpm for 1 min and dried at room temperature. Inside the glovebox, a 120 nm Ag cathode was deposited on top of the PEDOT:PSS layer through a shadow mask by thermal deposition. Photovoltaic performance was tested by a Newport AM 1.5 G solar simulator with AM 1.5 G type filter and optical mask. A Solarmeter digital radiometer was used to calibrate the incident solar intensity to 100 mW cm^{-2}. A Keithley source measure unit was used to record the corresponding data.

Measurement of Crack Onset Strains for OPV Active Layers on PDMS: Glass substrates (1 in. × 1 in.) were cleaned by ultrasonication sequentially with 0.5% Hellmanex III (Helma) in DI water, DI water, acetone, and isopropanol for 15 min and dried in an oven at 90 °C for 1 h. The substrates were then treated with UV–ozone for 15 min. PSS solution (20 mg mL^{-1}), which was prepared by dissolving 100 mg of PSS in 5 mL of deionized water, was spin-coated as a sacrificial layer on top of the glass substrate at 2000 rpm for 40 s and then dried at room temperature for 1 h. The active layer solution was spin-coated on top of the PSS layer at 2500 rpm for 20 s, cross-linked under UV short-wave irradiation, and dried at room temperature. PDMS was made by mixing silicone elastomer base with curing agent at 10:1 weight percent ratio in a Petri dish and was then cured at 90 °C for 3 h. Wet transfer technique was used to transfer active layer from glass to PDMS. The glass was placed on top of PDMS with active layer facing down. DI water was slowly dropped from the edge of glass and permeated through the substrate. After 20 min, the glass substrate was carefully lifted by a tweezer leaving the film behind on PDMS. Once the film on the PDMS substrate was dried, both ends of the substrate were clamped on a holder. Optical microscopy was then utilized to analyze cracks of the film to which uniaxial strains between 0 and 30% were applied.

Contact Angle Measurement: Contact angle measurement was conducted on drop shape analyzer from KRÜSS (DSA 100). A layer of film was spin-coated on glass substrate with 20 mg mL^{-1} PBDBT-2F:ITIC solution at 2500 rpm, 20 s. Sessile drops of PETMP, TPTMP, DPPA, and PAE were formed on the film, and respective contact angle were measured by the instrument.

Atomic Force Microscopy: Atomic force microscopy images were obtained in tapping mode with AFM NX20 from Park Systems.

Time-of-Flight Secondary Ion Mass Spectroscopy: Negative high mass resolution depth profile was performed using a ToF-SIMS NCS instrument, which combines a TOF.SIMS^5 instrument (ION-TOF GmbH, Münster, Germany) and an in situ Scanning Probe Microscope (NanoScan, Switzerland) at Shared Equipment Authority from Rice University. A bunched 30 keV Bi_3^+ ions (with a measured current of 0.2 pA) was used as primary probe for analyzing a field of view of 100 × 100 μm^2, with a raster of 128 × 128 pixels, and the sputtering was performed using Ar_{1500}^+ ions at 10 keV with a typical current around 1 nA, rastered area 500 × 500 μm^2. The beams were operated in non-interlaced mode, alternating two analysis cycles and one sputtering cycle (corresponding to 1.63 s) followed by a pause of 5 s for the charge compensation with an electron flood gun. An adjustment of the charge effects was operated using a surface potential. During the depth profiling, the cycle time was fixed to 200 μs (corresponding to m/z = 0–3645 a.m.u. mass range).

Supporting Information

Supporting Information is available from the Wiley Online Library or from the author.

Acknowledgements

Z.H., C.S., and R.V. acknowledge support from National Science Foundation under Grant No. DMR-1352099 and Welch Foundation under Grant No. C-1888. ToF-SIMS measurements were supported by the National Science Foundation under Grant No. CBET-1626418. ToF-SIMS analyses were carried out with support provided by the Shared Equipment Authority at Rice University.

Conflict of Interest

The authors declare no conflict of interest.

Author Contribution

Z.H. and C.S. contributed equally to this work. Z.H., C.S., and R.V. conceived and designed the analysis and wrote the paper. Z.H., C.S., and J.L. collected the data and performed the analysis. J.J., T.T., D.O., H.M., Y.L., Y.W., S.S., F.H., Y.Y., and A.M. contributed data and analysis tools.

Keywords

bending, crosslinked active layer, mechanical stability, organic photovoltaics

Received: March 25, 2020
Revised: June 14, 2020
Published online: July 6, 2020

[1] F. C. Krebs, M. Jørgensen, K. Norrman, O. Hagemann, J. Alstrup, T. D. Nielsen, J. Fyenbo, K. Larsen, J. Kristensen, *Sol. Energy Mater. Sol. Cells* **2009**, *93*, 422.
[2] M. Kaltenbrunner, M. S. White, E. D. Głowacki, T. Sekitani, T. Someya, N. S. Sariciftci, S. Bauer, *Nat. Commun.* **2012**, *3*, 770.
[3] A. M. Zamarayeva, A. E. Ostfeld, M. Wang, J. K. Duey, I. Deckman, B. P. Lechêne, G. Davies, D. A. Steingart, A. C. Arias, *Sci. Adv.* **2017**, *3*, e1602051.
[4] Y.-H. Lee, J.-S. Kim, J. Noh, I. Lee, H. J. Kim, S. Choi, J. Seo, S. Jeon, T.-S. Kim, J.-Y. Lee, J. W. Choi, *Nano Lett.* **2013**, *13*, 5753.
[5] S. Lee, Y. Lee, J. Park, D. Choi, *Nano Energy* **2014**, *9*, 88.
[6] S. Berny, N. Blouin, A. Distler, H.-J. Egelhaaf, M. Krompiec, A. Lohr, O. R. Lozman, G. E. Morse, L. Nanson, A. Pron, T. Sauermann, N. Seidler, S. Tierney, P. Tiwana, M. Wagner, H. Wilson, *Adv. Sci.* **2016**, *3*, 1500342.
[7] L. Ferlauto, M. J. I. A. Leccardi, N. A. L. Chenais, S. C. A. Gilliéron, P. Vagni, M. Bevilacqua, T. J. Wolfensberger, K. Sivula, D. Ghezzi, *Nat. Commun.* **2018**, *9*, 992.
[8] S. Park, S. W. Heo, W. Lee, D. Inoue, Z. Jiang, K. Yu, H. Jinno, D. Hashizume, M. Sekino, T. Yokota, K. Fukuda, K. Tajima, T. Someya, *Nature* **2018**, *561*, 516.
[9] D. J. Lipomi, Z. Bao, *Energy Environ. Sci.* **2011**, *4*, 3314.
[10] Q. Liu, Y. Jiang, K. Jin, J. Qin, J. Xu, W. Li, J. Xiong, J. Liu, Z. Xiao, K. Sun, S. Yang, X. Zhang, L. Ding, *Sci. Bull.* **2020**, *65*, 272.
[11] S. Savagatrup, A. D. Printz, T. F. O'Connor, A. V. Zaretski, D. Rodriquez, E. J. Sawyer, K. M. Rajan, R. I. Acosta, S. E. Root, D. J. Lipomi, *Energy Environ. Sci.* **2014**, *8*, 55.
[12] F. C. Krebs, T. D. Nielsen, J. Fyenbo, M. Wadstrøm, M. S. Pedersen, *Energy Environ. Sci.* **2010**, *3*, 512.
[13] D. J. Lipomi, B. C.-K. Tee, M. Vosgueritchian, Z. Bao, *Adv. Mater.* **2011**, *23*, 1771.
[14] M. Finn, C. J. Martens, A. V. Zaretski, B. Roth, R. R. Søndergaard, F. C. Krebs, D. J. Lipomi, *Sol. Energy Mater. Sol. Cells* **2018**, *174*, 7.
[15] R. Søndergaard, M. Hösel, D. Angmo, T. T. Larsen-Olsen, F. C. Krebs, *Mater. Today* **2012**, *15*, 36.
[16] B. Roth, S. Savagatrup, N. V. de los Santos, O. Hagemann, J. E. Carlé, M. Helgesen, F. Livi, E. Bundgaard, R. R. Søndergaard, F. C. Krebs, D. J. Lipomi, *Chem. Mater.* **2016**, *28*, 2363.
[17] S. Savagatrup, A. S. Makaram, D. J. Burke, D. J. Lipomi, *Adv. Funct. Mater.* **2014**, *24*, 1169.
[18] S. E. Root, S. Savagatrup, A. D. Printz, D. Rodriquez, D. J. Lipomi, *Chem. Rev.* **2017**, *117*, 6467.
[19] E. L. Melenbrink, K. M. Hilby, K. Choudhary, S. Samal, N. Kazerouni, J. L. McConn, D. J. Lipomi, B. C. Thompson, *ACS Appl. Polym. Mater.* **2019**, *1*, 1107.
[20] E. L. Melenbrink, K. M. Hilby, M. A. Alkhadra, S. Samal, D. J. Lipomi, B. C. Thompson, *ACS Appl. Mater. Interfaces* **2018**, *10*, 32426.
[21] T. Kim, J.-H. Kim, T. E. Kang, C. Lee, H. Kang, M. Shin, C. Wang, B. Ma, U. Jeong, T.-S. Kim, B. J. Kim, *Nat. Commun.* **2015**, *6*, 8547.
[22] G.-J. N. Wang, A. Gasperini, Z. Bao, *Adv. Electron. Mater.* **2018**, *4*, 1700429.
[23] J. W. Mok, Z. Hu, C. Sun, I. Barth, R. Muñoz, J. Jackson, T. Terlier, K. G. Yager, R. Verduzco, *Chem. Mater.* **2018**, *30*, 8314.
[24] W. Zhao, D. Qian, S. Zhang, S. Li, O. Inganäs, F. Gao, J. Hou, *Adv. Mater.* **2016**, *28*, 4734.
[25] H. J. Snaith, *Nat. Photonics* **2012**, *6*, 337.
[26] L. J. A. Koster, M. Kemerink, M. M. Wienk, K. Maturová, R. A. J. Janssen, *Adv. Mater.* **2011**, *23*, 1670.
[27] F. Liu, Y. Gu, X. Shen, S. Ferdous, H.-W. Wang, T. P. Russell, *Prog. Polym. Sci.* **2013**, *38*, 1990.
[28] Q. Liang, J. Han, C. Song, X. Yu, D.-M. Smilgies, K. Zhao, J. Liu, Y. Han, *J. Mater. Chem. A* **2018**, *6*, 15610.
[29] L. Huang, G. Wang, W. Zhou, B. Fu, X. Cheng, L. Zhang, Z. Yuan, Z. Yuan, S. Xiong, L. Zhang, Y. Xie, A. Zhang, Y. Zhang, W. Ma, W. Li, Y. Zhou, E. Reichmanis, Y. Chen, *ACS Nano* **2018**, *12*, 4440.
[30] M. D. Clark, M. L. Jespersen, R. J. Patel, B. J. Leever, *ACS Appl. Mater. Interfaces* **2013**, *5*, 4799.
[31] B. Vaughan, A. Stapleton, E. Sesa, N. P. Holmes, X. Zhou, P. C. Dastoor, W. J. Belcher, *Org. Electron.* **2016**, *32*, 250.
[32] J. Xu, H.-C. Wu, C. Zhu, A. Ehrlich, L. Shaw, M. Nikolka, S. Wang, F. Molina-Lopez, X. Gu, S. Luo, D. Zhou, Y.-H. Kim, G.-J. N. Wang, K. Gu, V. R. Feig, S. Chen, Y. Kim, T. Katsumata, Y.-Q. Zheng, H. Yan, J. W. Chung, J. Lopez, B. Murmann, Z. Bao, *Nat. Mater.* **2019**, *18*, 594.